Published in final edited form as:
J Phys Chem B. 2010 February 18; 114(6): 2293–2300. doi:10.1021/jp910219s.

How Amelogenin Orchestrates the Organization of Hierarchical Elongated Microstructures of Apatite

Xiudong Yang[†,¶], **Lijun Wang**[‡,¶], **Yueling Qin**[§], **Zhi Sun**[#], **Zachary J. Henneman**[†], **Janet Moradian-Oldak**[*,#], and **George H. Nancollas**[†,*]

[†] Department of Chemistry, The State University of New York at Buffalo, Amherst, New York 14260

[‡] College of Resources and Environment, Huazhong Agricultural University, Wuhan 430070, China

[§] Department of Physics, The State University of New York at Buffalo, Amherst, New York 14260

[#] Center for Craniofacial Molecular Biology, School of Dentistry, University of Southern California, Los Angeles, California 90033

Abstract

Amelogenin (Amel) accelerates the nucleation of hydroxyapatite (HAP) in supersaturated solutions of calcium phosphate (Ca-P), shortening the induction time (delay period), under near-physiological conditions of pH, temperature, and ionic strength. Hierarchically organized Amel and amorphous calcium phosphate (ACP) nanorod microstructures are formed involving co-assembly of Amel-ACP particles at low supersaturations and low protein concentrations in a slow, well-controlled, constant composition (CC) crystallization system. At the earliest nucleation stages, the CC method allows the capture of prenucleation clusters and intermediate nanoclusers, spherical nanoparticles, and nanochains prior to enamel–like nanorod microstructure formations at later maturation stages. Amel-ACP nanoscaled building blocks are formed spontaneously by synergistic interactions between flexible Amel protein molecules and Ca-P prenucleation clusters, and these spherical nanoparticles evolve by orientated aggregation to form nanochains. Our results suggest that, *in vivo*, Amel may determine the structure of enamel by controlling prenucleation cluster aggregation at the earliest stages by forming stable Amel-ACP microstructures prior to subsequent crystal growth and mineral maturation.

Keywords

amelogenin; apatite; biomineralization; kinetics of mineralization

Introduction

Tooth enamel is one of the hardest and most durable mineralized materials produced in vertebrates (1,2). Enamel structure shows complex hierarchical organization from the nanoscale to the macroscale involving building blocks (3), tightly packed carbonated fluorapatite nanorods in a species-specific manner by the predominant extracellular matrix protein, amelogenin (Amel) secreted by ameloblasts (4–6). The primary structures of mammalian Amels from bovine, porcine, human, mouse and rat have been determined, and the core domain of the protein appears to be well conserved (7–9). The nascent Amel molecule

*ghn@buffalo.edu; joldak@usc.edu Corresponding authors: George H. Nancollas, Tel: +1-716-645-4284. Fax: +1-716-645-6947; ghn@buffalo.edu; Janet Moradian-Oldak, Tel: +1-323-442-1759. Fax: +1-323-442-2981; joldak@usc.edu.
¶These authors contributed equally.

is bipolar, with a hydrophilic carboxyl terminus, but it is hydrophobic over most of its length (10). Recent bioinformatics analysis together with biophysical studies (CD and NMR) have classified Amel as a member of the intrinsically disordered or unstructured protein family (IDP) (11–13).

Much evidence shows that Amel self-assembles to form supermolecular nanospheres that facilitate the organization of inorganic nanostructures in developing enamel crystals (14), and there is general agreement that Amel plays a critical role in templating and crystallizing HAP, especially for the initial nucleation in vitro (15,16). However, the mechanisms by which Amel is able to nucleate and direct oriented crystal growth *in vitro* remain unclear. *In vitro* preparation of biomaterials that resemble enamel is of a great interest in the field of material science and dentistry (17,18). In an attempt to synthesize such materials, investigators have applied different *in vitro* crystallization approaches to mimic the formation of enamel-like microstructures in the presence of Amel (17,19–21) and other organic additives such as gels, surfactant/polymer and protein/peptide systems (22–25). However, these *in vitro* studies have not focused on the initial contact between mineral nuclei/clusters and organic additives that drive the earliest nucleation/aggregation events responsible for subsequent directed assembly, to yield the complex morphologies and mineral microstructures found in enamel. Moreover, the relatively high supersaturations used in these studies inevitably obscured the nucleation events that would take place in a slow crystallization process (26). Our recent studies have taken a different route by lowering experimental concentrations to slow down crystallization, and by investigating HAP nucleation at physiological pH and temperature in a well-controlled constant composition (CC) crystallization system (27,28). The promotion of calcium phosphate (Ca-P) nucleation by the full-length recombinant Amel (rP172) at relatively low supersaturations has provided some possible clues about the cooperative formation of composite spherical particles of nanocrystallite apatite and Amel in the initial nucleation stages (27,28). The composite nanoparticles then aggregate into nanorods that in turn, further assemble to form organized, elongated crystals that begin to resemble biological enamel (27, 28).

To date, little is known about the exact crystallization pathways from solvated ions through nuclei or clusters to the final apatitic mineral phase, nor has the potential existence of anticipated intermediate stable phases been explored for nucleation in Ca-P supersaturated solutions to which Amel had been added. We have developed CC crystallization techniques uniquely suited for monitoring the earliest nucleation/aggregation stages for Ca-P crystallization under precisely defined thermodynamic driving forces and near-physiological conditions (27,28). This newly developed CC method, sensitive to ion concentration changes at the nanomolar level (29), yields reproducible experimental induction periods for both HAP and other Ca-P phases and enables nucleation/aggregation and growth reactions to be investigated at very low thermodynamic driving forces, an essential requirement for probing the earliest nucleation/aggregation events. Herein we report that, in solutions closer to the physiological microenvironment and having HAP stoichiometry at low supersaturation (σ_{HAP}=15.1, ionic strength=0.15 M, 37 °C, and pH 7.40), Amel kinetically promotes Ca-P nucleation/aggregation by decreasing the induction time for spontaneous nucleation, and that Amel/ACP nanospherical building blocks are formed by synergistic interactions between the flexible Amel protein molecules and the prenucleation Ca-P clusters. The nanorod microstructures were successfully captured following the formation of the co-assembled Amel-ACP nanochains, another intermediate phase, at the earliest nucleation stages. In addition, the hidden fine nanostructures contained within the ordered, elongated HAP crystals detected at later CC growth stages, provide supplemental evidence for the multistep co-assembly process and a possible pathway to enamel biomineralization.

Results

The nucleation and subsequent crystal growth in the presence of the full-length recombinant Amel at 25 μg mL^{-1} have been investigated in the CC system, and the mineral phases at different crystallization stages were characterized using SEM and HRTEM. Figure 1a shows representative CC curves of titrant addition as a function of induction time for HAP crystallization in the absence and presence of full-length Amel. The induction time for pure supersaturated solution was 830 ± 50 min (n=3). However, in the presence of full-length Amel at 25 μg mL^{-1}, this decreased to 268 ± 50 min (n=3). The presence of the 25 amino acid C-terminus polypeptide of Amel in the same supersaturated Ca-P solution did not influence the induction time (data not shown). Randomly aggregated HAP crystallites were grown in the absence of Amel (Figure 1b), whereas in its presence, ordered, elongated structures with a higher aspect ratio (Figure 1c) were recovered from the bulk solution by filtration following the shortened induction period. Energy dispersive spectrometry (EDS) revealed a Ca/P molar ratio of 1.63 ± 0.03 (n=3) (Inset in Figure 1b) for the randomly aggregated HAP crystallites and a Ca/P molar ratio of 1.52 ± 0.05 (n=3) (Inset in Figure 1c) for the elongated crystallites.

FTIR was used to obtain an independent bulk estimate of the mineral. FTIR spectra in Figure 1d (in blue) show the characteristic peaks of protein and phosphate groups, suggesting that the elongated crystallite is an inorganic-organic composite material. Note the presence of amide peaks, I (1654 cm^{-1}) II (1543 cm^{-1}) and III (1202 cm^{-1}), and -CH_2- bending modes (1441 cm^{-1}) (Figure 1d in red) (30, 31). The bands at 1096, 1035, 961, 603 and 562 cm^{-1} derived from PO_4 modes of HAP were also present in this spectrum (Figure 1d in green). Compared with the FTIR results of pure lyophilized Amel and the Ca-P-Amel composite, the shifts of the Amide I (from 1654 to 1629 cm^{-1}), Amide II (from 1543 to 1523 cm^{-1}, Amide III (from 1202 to 1231 cm^{-1}) and CH_2 bending (from 1441 to 1461 cm^{-1}) may be associated with secondary structural changes following the interaction between Amel and Ca-P (Figure 1d in blue) (30, 31). The presence of broader peaks at around 1035 cm^{-1} and 562–603 cm^{-1} indicates the presence of an amorphous Ca-P phase (Figure 1d in blue) (30, 31).

Interestingly, the hidden fine nanostructures contained within the elongated HAP crystals were observed in broken HAP crystals (Figure 2a; n=3) which had exposed bundles of pearl-like nanothreads (Figure 2b). Each nanothread consisted of 30–50 nm nanoparticles connected to each other as shown within the dotted rectangles in Figure 2c. The nanothreads were aligned in parallel to form elongated micro-sized HAP crystals with a higher aspect ratio, and are compositionally and morphologically similar to crystallites isolated from natural enamel (32). The EDS spectrum revealed a Ca/P molar ratio of 1.50 ± 0.04 (n=3) for the pearl-like nanothreads (Inset in Figure 2b).

To further investigate how these elongated microstructures are formed under the influence of Amel, well controlled free drift experiments were made without titrant addition to monitor pH changes to within 0.002 units at the earliest CaP aggregation stages. Figure 3 shows that, during a 268 min initial induction period in the presence of 25 μg mL^{-1} Amel, the pH (7.400) remained constant for ~130 min (stage A_I), slowly increased by ~0.013 pH units over an 80 min time period (Stage A_{II}), and then slowly returned to 7.400 over the next 60 min (Stage A_{III}). This was followed by a more rapid pH reduction to <7.320 (Stage A_{IV}, Figure 3). The kinetic nature of the pH changes was confirmed by the control experiments shown in Figure 3. pH changes in the absence and presence of Amel prior to stage IV were symmetric, suggesting that the time required for the pH to reach the maximum value was approximately the same as that for the pH to return to 7.400. However, time periods for stages A_{II} and A_{III} (each stage, 60 min) in the presence of Amel were significantly shorter than either C_{II} and C_{III} (each 300 min) in the absence of Amel. This clearly demonstrates the role of Amel in promoting nucleation of calcium phosphate phases in both stages II and III.

Corresponding HRTEM measurements of the different stages of pH change were made during inorganic phase formation. In pure Ca-P supersaturated solutions, nanoclusters with dimensions of 2.0–5.0 nm (Figure 4a) were observed in stage C_{III} (no solid phases were observed prior to stage C_{III}), and these nanoclusters assembled into globular ACP nanoparticles of irregular size distribution (~30 nm) early in the C_{IV} period (Figures 4b, c); crystalline particles then formed simultaneously from bulk ACP (Figure 4c). Selected area electron diffraction (SAED) showed that numerous crystallites had developed from the aggregated ACP (stage C_{IV}) after maturation times of ~2 hrs (Figure 4d), suggesting that the rapid drop in pH at stage IV reflects a phase transformation from ACP to HAP. However, ACP was present throughout all four stages, even extending to 24 hrs.

In CC supersaturated solutions to which Amel had been added, striking intermediate nanostructures were captured by HRTEM (Figures 4e–k). In stage A_I, prenucleation Ca-P clusters of ~1.0 nm in diameter were observed (Figure 4e). At stage A_{II}, Figures 4f & 4g show 2.0–10.0 nm Ca-P clusters, while at stage A_{III} spherical nanoparticles with sizes 30–50 nm (Figure 4h) gradually assembled into elongated pearl-like nanochains during stage A_{IV} (Figure 4h). Phase transformations of the Amel-Ca-P composite nanochains from amorphous to crystalline were confirmed using continuous TEM examination (data not shown).

Sampling of the supersaturated solutions containing Amel revealed that the intermediate phases including nanoclusters, spherical nanoparticles, and nanochains were metastable. After a 2h growth period at stage A_{IV}, bundles of the ribbonlike crystals with preferentially oriented *c*-axes were formed (Figure 4i), and the SAED patterns corresponded to the (002) plane for HAP (Inset, Figure 4i). Further maturation extending to 24 h revealed the formation of uniform-sized nanorods resembling those of tooth enamel crystallites (Figure 4j). SAED examination confirmed preferential alignment of the HAP crystallographic *c*-axes along the long axes of the nanorods (Inset, Figure 4j). The measured lattice spacing of 0.346 nm, by HRTEM, corresponded to the (002) HAP lattice plane (Figure 4k) (27).

Dynamic Light Scattering (DLS) measurements revealed the particle size evolution for Ca-P supersaturated solutions in the presence of 25 μg $mL^{-}1$ Amel (Figure 5). At the earlier A_I stage, clusters with a R_H of 0.8–1.4 nm were present in relatively high abundance, in addition to larger Amel assemblies with a R_H of 60–80 nm (Figure 5a). In stage A_{II}, the quantity of nanoparticles with a R_H of ~10–40 nm (Figure 5b) clearly increased as compared with stage A_I. Additional DLS measurements were made for a solution containing Amel (25 μg mL^{-1}) but without calcium and phosphate ions, and compared to a Ca-P supersaturated solution without Amel. In the former solution (Amel, no Ca-P), clusters with a diameter of ≤1.0 nm were undetectable, whereas small diameter clusters (2 nm < R_H < 10 nm) were present in low abundance, and larger spheres (R_H >10 nm) were observed in moderate abundance (Figure 5c); these observations have also been shown by Moradian-Oldak *et al*. (33). In the latter case (no Amel, supersaturated with Ca-P), no stable uniform sized particles were observed, and thus no DLS data were available.

Discussion

The results of CC-HAP crystallization experiments in the presence of Amel can be divided into two stages: (1) controlled aggregation, and (2) organized post-nucleation crystal growth involving a stepwise hierarchical co-assembly of Amel-Ca-P nanoclusters. This is schematically presented in Fig. 6., where Amel first captures and stabilizes the Ca-P clusters, then controls the organization and morphology of the ACP nanostructures, followed by gradual transformation of the amorphous phase into the final crystalline phase. Controlled aggregation of primary-composite nanoclusters takes place at relatively low supersaturation, forming spherical nanoparticles. As first building blocks, these co-assemble into organized elongated

pearl-like nanochains. As secondary building blocks, these further co-assemble into Amel-ACP nanoribbons or nanorods. In the post-nucleation crystal growth stages, these nanorods further evolve into the final organized, elongated HAP crystalline phase (Figure 6). In contrast, nucleation in supersaturated solutions in the absence of Amel produces random Ca-P clusters and nuclei which aggregate to form bulk ACP, which subsequently transforms into randomly oriented, aggregated HAP crystallites. In stage IV (A_{IV} and C_{IV}, Figure 3), HAP crystal growth follows classical crystallization theory, thermodynamic and kinetic control involving Ostwald ripening.

The basic structure of mature tooth enamel can be represented by a dense array of carbonated-fluorapatite nanorods with their crystalline *c*-axes parallel to the nanorods (34). It has been suggested that elongated ribbon-like crystals in early secretory enamel form via fusion of spherical particles containing ACP and protein (6,35–38). Interestingly, the size, shape and spatial organization of these amorphous mineral nanoparticles and crystals are essentially the same, indicating that the mineral morphology and organization at the early stage of enamel formation is determined prior to its crystallization (39). However, besides the amorphous phase, the question whether or not other transient mineral phases such as octacalcium phosphate (OCP) exist in forming enamel prior to the final carbonated apatite (CAP) remains unsolved (40). *In vivo*, transient mineral phases could be controlled by macromolecules, such as amelogenins and their proteolytic products, as well as non-amelogenin proteins and other small ions; the phase transformations and stabilities of these phases are pH-dependent (41).

In this *in vitro* CC study, the pH changes during the earliest stages of nucleation directly suggest that clusters, formed as soon as the supersaturated solutions are prepared at pH 7.40 and ionic strength 0.15 M, may either dissolve or aggregate. Aggregation leads to globular ACP formations, most of which would dissolve, leading to an increase in pH (stages A_{II} and C_{II}, Figure 3). At the same time, the pH will decrease when ACP begins to precipitate from solution due to the release of protons (stages A_{III} and C_{III}, Figure 3), and other mineral phases appear. Calcium-phosphates are highly polymorphic, and the first polymorph formed following nucleation is often ACP, which subsequently undergoes crystallization (41,42); this was shown in forming enamel by Beniash *et al* (39). Mahamid *et al.* also demonstrated an abundance of amorphous Ca-P phase in newly formed fish bones, which may be a precursor to mature crystalline mineral (43). Posner suggested that precipitated ACP consists of aggregates of primary nuclei (roughly spherical clusters) with composition $Ca_9(PO_4)_6$ (Ca/P molar ratio of 1.50), the so called “Posner’s clusters (PC)” (44). These pre-critical clusters were presumed to pack randomly, forming 30–80 nm nanoparticles (45). If metastable pre-critical clusters exist they must lie in a free energy minimum, the structure and depth of which remains unknown (46). Interestingly, the formation of these clusters may help to lower the activation barriers for crystal nucleation and growth of the metastable polymorph (47). Once such metastable crystals grow, a separate set of nucleation events and/or a dissolution-reprecipitation mechanism corresponding to the pH changes in Stages II and III (Figure 3) may be required to form a subsequent more stable phase.

The observed pre-critical clusters were amorphous (‘non-crystalline’ (44)) or of low structural order, and it is important to understand how they were able to remain relatively stable. The most likely scenario is that they were stabilized for a period of time by Amel, which provided an opportunity for stabilization of the pre-critical clusters in a free energy minimum; this mechanism does not contradict classical nucleation theory (42,48). Kwak *et al.* showed that both non-phosphorylated full-length Amel rP172 and phosphorylated Amel P148 lacking the hydrophilic C-terminal tail of 25 amino acids, stabilized ACP nanoparticles that were found to re-align to form linear needle-like particles, which subsequently transformed and organized into parallel arrays of apatitic needle-like crystals (49). In addition, the peptide motifs present in Dentin Matrix Protein 1 (DMP1) facilitated reorganization of the internal structure of

amorphous Ca-P nanoparticles/nanoclusters into ordered crystalline states (50). This transformation was attributed to the organization of liquid-like, pre-critical clusters into the amorphous spherical particles/nanochains and the ordered crystalline nanorods (Figures 4,6). Since the amorphous phase with larger degrees of freedom is more easily molded and re-arranged by biomacromolecular assemblies, it is also likely that the labile structure of Amel protein facilitates such macromolecular assembly and/or subsequent organic-inorganic co-assembly (13). This crystallization mechanism is in accordance with the two-step crystallization model (TSC) (42,51–54).

It is unfortunately difficult to acquire independent evidence to suggest that all nanorods are converted to final elongated HAP crystals under our *in vitro* CC solution conditions. This has been due in part to the limitations of existing experimental approaches for monitoring *in situ* and time-resolved particle evolution. The transformation from nanorods (Figure 4j) to elongated HAP crystals (Figures 1c and 2) is thought to be closely related to the careful selection of thermodynamic driving force conditions for the CC HAP crystallization experiments. It has been suggested that a self-epitaxial nucleation-mediated assembly mechanism would explain the parallel aligned nanorods (Figure 4j) that further assemble into the well organized and elongated microstructures (26, 28, 55, 56).

Conclusions

Our study emphasizes that the earliest stage of crystallization usually directs the remainder of the growth process, and demonstrates that the crystallization pathway from solvated ions to prenucleation clusters ($R_H \approx 1–10$ nm) (Figures 4e and f), then to intermediate nanochains (Figure 4h) and nanorods (Figure 4j), is similar to that for natural enamel rods prior to the final formation of elongated HAP crystals (Figures 1c and 2). It is difficult to relate entirely our *in vitro* results to *in vivo* enamel formation, because of differences between the solution conditions used in our CC crystallization system and those found in the physiological microenvironment within enamel extracellular matrix. However, this study takes a further step toward the development of an in-depth physical-chemical understanding of how Amel controls prenucleation cluster aggregation during the earliest stages of Ca-P mineralization, and how hierarchical HAP microstructures are formed from metastable Amel-ACP phases. Hierarchical co-assembly of Amel-ACP particles gives rise to a remarkably high degree of cooperativity at low driving force. Under cooperative kinetic control, the co-assembly of Amel-Ca-P clusters plays an explicit role in directing Amel/ACP nanoparticles towards the final elongated crystalline structure. Formation of the primary building blocks (nanocluster composites) probably imparts kinetic and thermodynamic stability to the system, which may lower the free energy barrier to formation of secondary structures of intermediate phases (Amel/ACP nanosphere chains and nanorods), which ultimately undergo phase transformation to the final crystalline phase of mature enamel (elongated HAP).

Experimental Section

Preparation of Recombinant Porcine Amel rP172

Recombinant amelogenin rP172 was expressed in Escherichia coli strain B121(DE3) and purified by ammonium sulfate precipitation, and reverse-phase column chromatography (214TP510, Vydac, Separation Group) as previously described (57,58). rP172 has 172 amino acids and is an analog of the full-length native porcine P173, lacking the N-terminal methionine and a phosphate group on Ser16.

Constant Composition (CC) HAP Crystallization

CC experiments were made in magnetically stirred double-walled Pyrex vessels. In this study, hydroxyapatite (HAP, $Ca_{10}(PO_4)_6(OH)_2$) crystallization experiments in the presence of Amel were made at 37.0 ± 0.1°C and the constancy of solution compositions during the experiments was verified as described previously (27). The relative supersaturation, σ, and supersaturation ratio, *S,* are given by eq 1:

$$\sigma = S - 1 = \left(\frac{IAP}{K_{sp}}\right)^{1/v} - 1 \quad (1)$$

in which *v* (=18) is the number of ions in a formula unit of HAP, and *IAP* and K_{sp} are the ionic activity and thermodynamic solubility product (K_{sp}=5.52 × 10^{-118} mol^{18} L^{-18} at 37.0°C) respectively (32). Solution speciation calculations were made using the extended Debye-Hückel equation proposed by Davies (32). Supersaturated reaction solutions (normally consisting of [$CaCl_2$]=1.80 mmol L^{-1}, [KH_2PO_4]=1.08 mmol L^{-1}, [KOH]=0.907 mmol L^{-1} and [NaCl]=0.142 mol L^{-1} for σ_{HAP} = 15.1 at pH=7.400) were prepared by the slow mixing of calcium chloride (0.020 mol L^{-1}) and potassium dihydrogen phosphate (0.020 mol L^{-1}) with sodium chloride to maintain an ionic strength *I* = 0.150 mol L^{-1}. Amel protein (25.0 μg mL^{-1}) was added to the supersaturated reaction solutions. The pH during crystallization experiments was monitored by a pH electrode (Orion 91-01) coupled with a single-junction Ag/AgCl reference electrode (Orion 90-01). The output of the potentiometer (Orion 720A) was constantly compared with a preset value, and a difference in hydrogen ion activities, or error signal (± 0.05 mv) triggered the addition of titrant.

SEM and HRTEM Observation

Crystallites were collected from each reaction solution by vacuum filtration, were dried, and samples were sputter-coated with carbon under vacuum for examination by field-emission scanning electron microscopy (SEM, Hitachi S-4000) at 20Kev. High-resolution transmission electron microscopy (HRTEM) investigations of nucleated particles removed at various time intervals were carried out using a JEOL-2010 TEM at an accelerating voltage of 200 kv.

Fourier-transform Infrared (FTIR) Spectroscopic Analysis

Ca-P/Amel composite samples were collected by filtration and prepared in dried KBr at a ratio of 1:200 in a die, under hydraulic pressure (12 tonnes/2 min). FTIR spectra were collected (Perkin Elmer, Wellesley, MA, USA) by integrating 1024 scans at the resolution of 4 cm^{-1}, recorded in the range 2000-400cm^{-1} to observe protein bands. Additional independent FTIR analyses of Ca-Ps and recombinant rP172 Amel were also made using the same method.

Dynamic Light Scattering (DLS) Measurements

Particle size distributions of rP172 at different solution conditions were systematically analyzed using a Malvern Zetasizer nano-ZS90 dynamic light scattering instrument (Malvern Instruments, UK), operating at a wavelength of 633 nm at a controlled temperature of 37°C, scattering angle of 90°, in covered quartz cells to maintain the solution conditions, with a particle size detection limit of 1.0 nm–3.0 μm, as previously described (27). Data for each experiment were collected at 1.0 min intervals over a 500 min time period. The detected hydrodynamic radii from the individual runs were grouped into 10 categories: <1.0, 1.0–1.5, 1.5–2.0, 2–10, 10–40, 40–60, 60–80, 80–100, 100–200, and >200 nm. The occurrence rates of different categories were used to represent the particle size distribution in this heterogeneous system.

Acknowledgments

This work was supported by NIH Grants DE003223 to G.H.N. and DE013414 and DE015644 to J.M.-O. We thank Dr. Daming Fan for assistance in protein expression and purification.

References

1. Lowenstam HA. Science 1981;211:1126–1131. [PubMed: 7008198]
2. Moradian-Oldak, J.; Paine, ML. Biomineralization. From Nature to Application. In: Sigel, A.; Sigel, H.; Sigel, RKO., editors. Metal Ions In Life Sciences Series 4. John Wiley & Sons; Chichester: 2008. p. 507-546.
3. Lowenstam, HA.; Weiner, S. On Biomineralization. Oxford Univ. Press; Oxford: 1989.
4. Diekwisch TGH, Berman BJ, Gentner S, Slavkin HC. Cell Tissue Res 1995;279:149–167. [PubMed: 7895256]
5. Moradian-Oldak J, Du C, Falini G. Eur J Oral Sci 2006;114:289–296. [PubMed: 16674701]
6. Margolis HC, Beniash E, Fowler CEJ. J Dent Res 2006;85:775–793. [PubMed: 16931858]
7. Aoba T, Moreno EC, Kresak M. J Dent Res 1989;68:1331–1336. [PubMed: 2778177]
8. Moradian-Oldak J, Simmer JP, Lau EC, Sarte PE, Slavkin HC, Fincham AG. Biopolymers 1994;34:1339–1347. [PubMed: 7948720]
9. Sidney D, Didier C, Laure B, Michel L, Jean-Yves S, Marc G. Mol Biol Evol 2001;18:2146–21531. [PubMed: 11719563]
10. Toyosawa S, O'hUigin C, Figueroa F, Tichy H, Klein J. Proc Natl Acad Sci USA 1998;95:13056–13061. [PubMed: 9789040]
11. Lakshminarayanan R, Fan D, Du C, Moradian-Oldak J. Biophys J 2007;93:3664–3674. Erratum in Biophys J. 2008, 94, 715. [PubMed: 17704165]
12. Lakshminarayanan R, Yoon I, Hedge BG, Fan D, Du C, Moradian-Oldak J. Proteins 2009;76:560–569. [PubMed: 19274734]
13. Delak K, Harcup C, Lakshminarayanan R, Sun Z, Fan Y, Moradian-Oldak J, Evans JS. Biochemistry 2009;48:2272–2281. [PubMed: 19236004]
14. Moradian-Oldak J. J Dent Res 2007;86:487–490. [PubMed: 17525347]
15. Tarasevich BJ, Howard CJ, Larson JL, Snead ML, Simmer JP, Paine M, Shaw WJ. J Cryst Growth 2007;304:407–415.
16. Tao JH, Pan HH, Zeng YW, Xu XR, Tang RK. J Phys Chem B 2007;111:13410–13418. [PubMed: 17979266]
17. Fan Y, Sun Z, Moradian-Oldak J. Biomaterials 2009;30:478–483. [PubMed: 18996587]
18. Moradian-Oldak J. Dimensions of Dental Hygiene 2009;7:12–15.
19. Hunter GK, Curtis HA, Grynpas MD, Simmer JP, Fincham AG. Calcif Tissue Int 1999;65:226–231. [PubMed: 10441656]
20. Habelitz S, Kullar A, Marshall SJ, DenBesten PK, Balooch M, Marshall GW, Li WJ. J Dent Res 2004;83:698–702. [PubMed: 15329375]
21. Fan Y, Sun Z, Wang R, Abbott C, Moradian-Oldak J. Biomaterials 2007;28:3034–3042. [PubMed: 17382381]
22. Busch S. Angew Chem Int Ed 2004;43:1428–1431.
23. Tlatlik H, Simon P, Kawska A, Zahn D, Kniep R. Angew Chem Int Ed 2006;45:1905–1910.
24. Fowler CE, Li M, Mann S, Margolis HC. J Mater Chem 2005;15:3317–3325.
25. Chen HF, Clarkson BH, Sun K, Mansfield JF. J Colloid Interface Sci 2005;288:97–103. [PubMed: 15927567]
26. Jiang HD, Liu XY. J Biol Chem 2004;279:41286–41293. [PubMed: 15192103]
27. Wang LJ, Guan XY, Du C, Moradian-Oldak J, Nancollas GH. J Phys Chem C 2007;111:6398–6404.
28. Wang LJ, Guan XY, Yin HY, Moradian-Oldak J, Nancollas GH. J Phys Chem C 2008;112:5892–5899.
29. Tomson MB, Nancollas GH. Science 1978;200:1059–1060. [PubMed: 17740700]

30. Elangovan S, Margolis HC, Oppenheim FG, Beniash E. Langmuir 2007;23:11200–11205. [PubMed: 17880251]
31. Shirkhanzadeh M. J Mater Sci Mater Med 1995;6:90–93.
32. Wang LJ, Tang RK, Bonstein T, Bush P, Nancollas GH. J Dent Res 2006;85:359–363. [PubMed: 16567559]
33. Moradian-Oldak J, Leung W, Fincham AG. J Struct Biol 1998;122:320–327. [PubMed: 9774536]
34. Ten Cate, AR. Oral Histology: Development, Structure and Function. Mosby; St. Louis: 1985.
35. Robinson C. J Dent Res 2007;86:677–679. [PubMed: 17652193]
36. Robinson C, Shore RC, Wood SR, Brookes SJ, Smith DAM, Wright JT, Connell S, Kirkham J. Connect Tissue Res 2003;44:65–71. [PubMed: 12952176]
37. Robinson C, Fuchs P, Weatherell JA. J Cryst Growth 1981;53:160–165.
38. Travis DF, Glimcher MJ. J Cell Biol 1964;23:447–497. [PubMed: 14245432]
39. Beniash E, Metzler RA, Lam RSK, Gilbert PUPA. J Struc Biol 2009;166:133–143.
40. Aoba T, Komatsu H, Shimazu Y, Yagishita H, Taya Y. Connect Tissue Res 1998;38:129–137. discussion 139–145. [PubMed: 11063022]
41. Wang LJ, Nancollas GH. Chem Rev 2008;108:628–4669.
42. Wang LJ, Nancollas GH. Dalton Trans 2009:2665–2672. [PubMed: 19333487]
43. Mahamid J, Sharir A, Addadi L, Weiner S. Proc Natl Acad Sci USA 2008;105:12748–12753. [PubMed: 18753619]
44. Eanes ED, Gillessen IH, Posner AS. Nature 1965;208:365–367. [PubMed: 5885449]
45. Betts F, Posner AS. Trans Am Crystallogr Assoc 1974;10:73–84.
46. Gebauer D, Völkel A, Cölfen H. Science 2008;322:1819–1822. [PubMed: 19095936]
47. Navrotsky A. Proc Natl Acad Sci USA 2004;101:12096–12101. [PubMed: 15297621]
48. Meldrum FC, Sear RP. Science 2008;322:1802–1803. [PubMed: 19095931]
49. Kwak SY, Wiedemann-Bidlack FB, Beniash E, Yamakoshi Y, Simmer JP, Litman A, Margolis HC. J Biol Chem 2009;284:18972–18979. [PubMed: 19443653]
50. Tsuji T, Onuma K, Yamamoto A, Iijima M, Shiba K. Proc Natl Acad Sci USA 2008;105:16866–16870. [PubMed: 18957547]
51. ten Wolde PR, Frenkel D. Science 1997;277:1975–1978. [PubMed: 9302288]
52. Addadi L, Weiner S. Angew Chem Int Ed 1992;31:153–169.
53. Chen XB, Samia ACS, Lou YB, Burda C. J Am Chem Soc 2005;127:4372–4375. [PubMed: 15783219]
54. Zhang TH, Liu XY. J Am Chem Soc 2007;129:13520–13526. [PubMed: 17929918]
55. Jiang HD, Liu XY, Zhang G, Li Y. J Biol Chem 2005;280:42061–42066. [PubMed: 16251185]
56. Jiang HD, Liu XY, Lim CT, Hsu CY. Appl Phys Lett 2005;86:163901–163903.
57. Moradian-Oldak J, Jimenez I, Maltby D, Fincham AG. Biopolymers 2001;58:606–616. [PubMed: 11285557]
58. Ryu OH, Fincham AG, Hu CC, Zhang C, Qian Q, Bartlett JD, Simmer JP. J Dent Res 1999;78:743–750. [PubMed: 10096449]

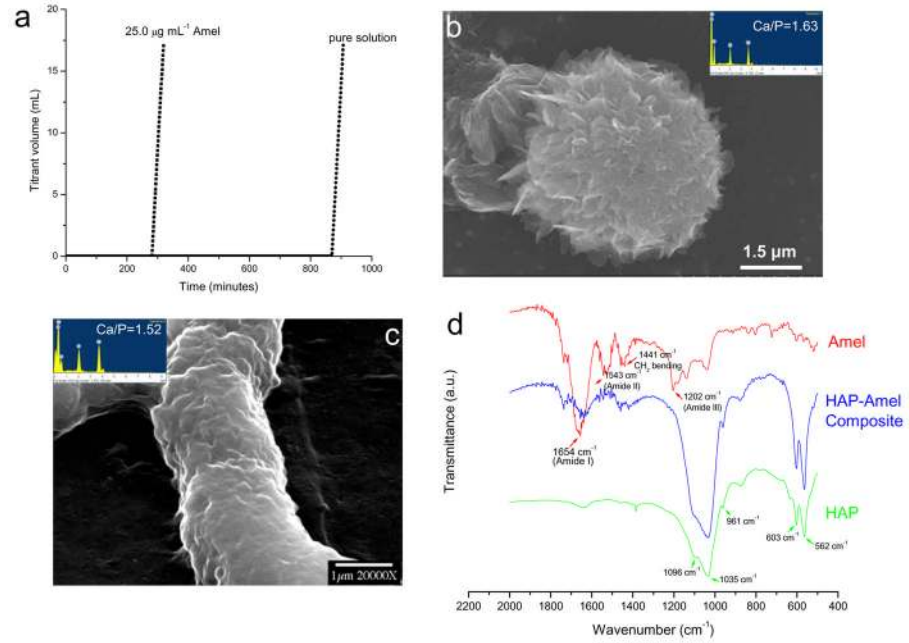

Figure 1.

CC HAP crystallization (σ_{HAP}=15.1, pH=7.40 and 37.0°C) and crystal characterization. (a) Representative CC plots of titrant addition as a function of time for HAP crystallization in the absence and presence of 25.0 μg mL^{-1} Amel. SEM micrographs of (b) randomly aggregated HAP crystallites in the absence of Amel, and (c) an ordered and elongated crystal formed in the presence of Amel at 25.0 μg mL^{-1}. The insets in (b) and (c) are EDS results from crystals collected from the bulk solution by filtration following the long induction periods. (d) FTIR spectra of the elongated HAP crystals, demonstrating the presence of protein and PO_4 groups.

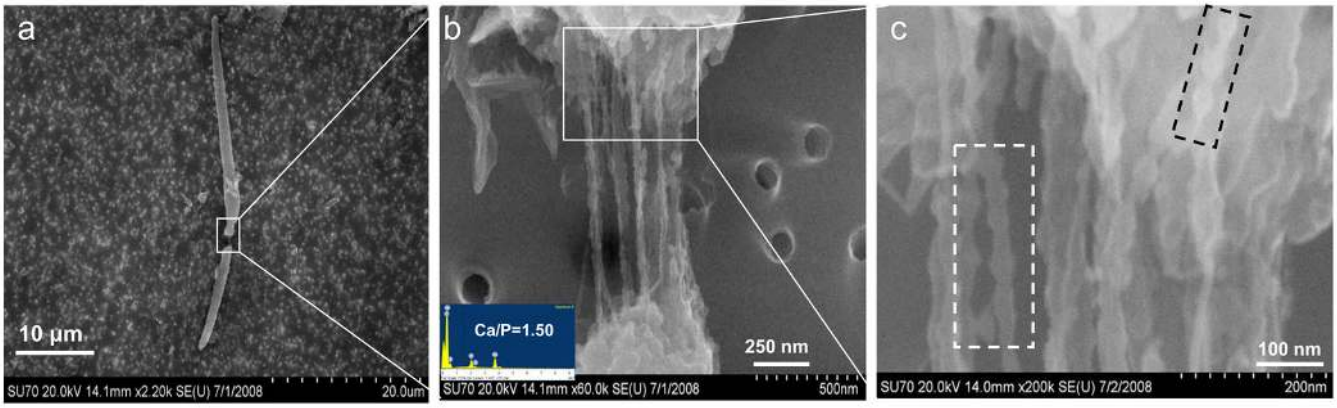

Figure 2.

SEM images of fine nanostructures contained within an elongated HAP crystal, isolated following an ~300 min induction period. (a) Fractured HAP crystal collected from the CC bulk solution by filtration. (b) An enlarged area of (a), revealing that elongated HAP crystals consist of bundles of pearl-like nanothreads. The inset EDS was recorded from the rectangle in (b), showing a Ca/P ratio of 1.50 ± 0.04 (n=3). (c) Nanoparticles (30–50 nm) are connected to each other to form the nanothreads as shown within two dotted rectangles in (c).

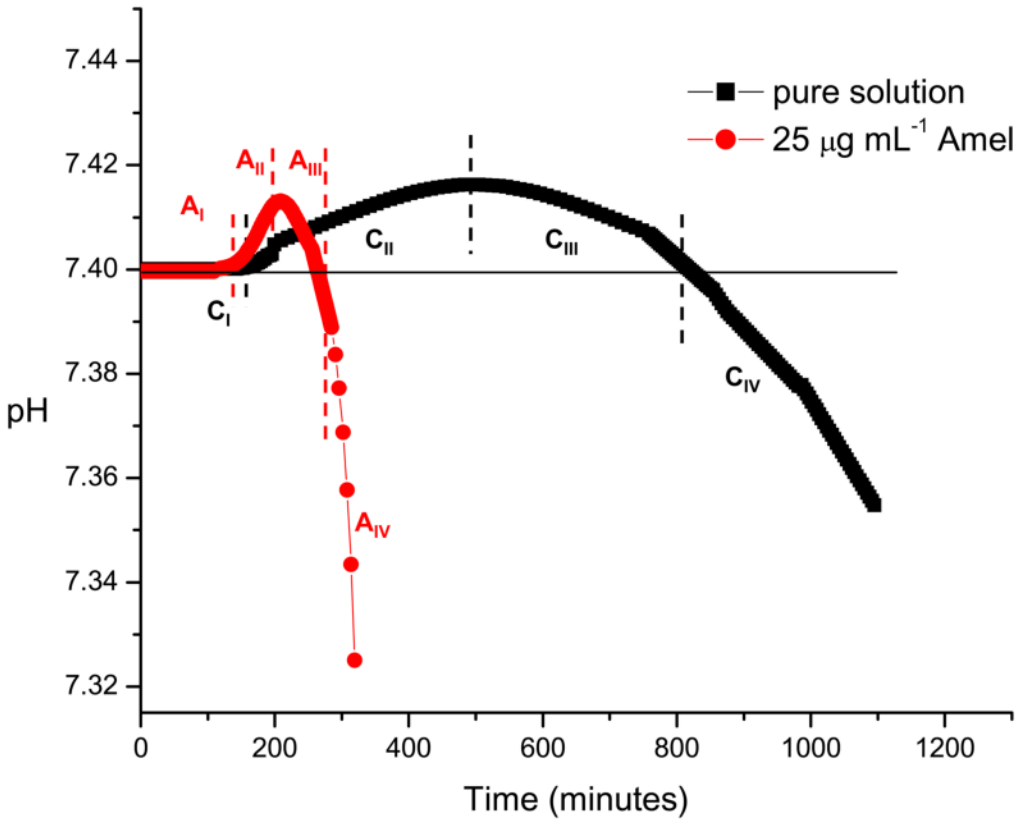

Figure 3.
pH curves for HAP crystallization experiments made at σ_{HAP}=15.1, pH=7.400 and 37 °C (free drift experiments, no titrant addition) in the absence (C_I – C_{IV}) and presence (A_I – A_{IV}) of 25 μg mL^{-1} full-length Amel. Typical stages of crystallization (I, II, III, and IV) correspond to the various pH changes described in the text.

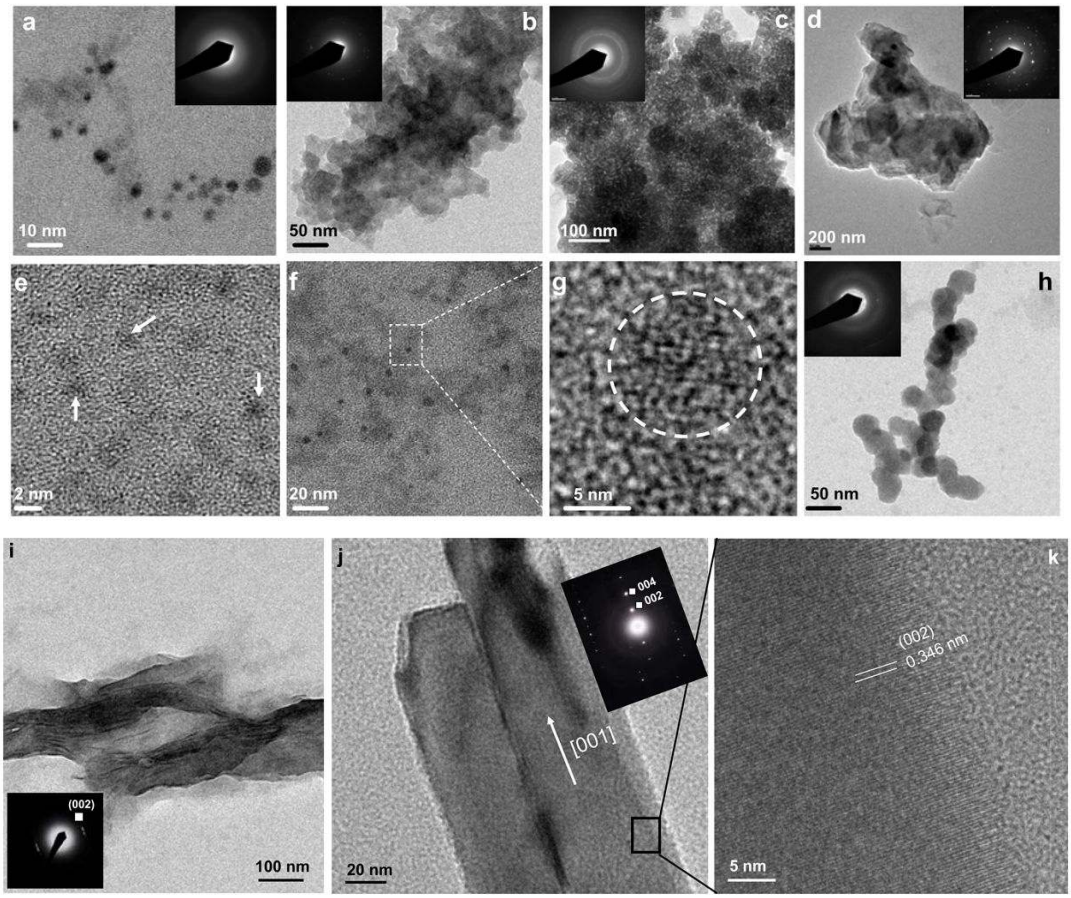

Figure 4.

High Resolution TEM images of Ca-P inorganic phases extracted at the indicated stages (I-IV) of the corresponding pH profiles in the absence (a–d) and presence (e–k) of 25 μg mL^{-1} Amel. (a) 2.0–5.0 nm clusters/particles collected in stage C_{III}. The inset shows the SAED pattern of the amorphous nanoclusters/nanoparticles. (b, c) Nanoclusters aggregated into spherical particles of hydrated ACP in stage C_{IV}, and the weak diffracted rings (inset in c) suggest that crystalline particles formed simultaneously from the bulk ACP. (d) Numerous crystallites developed from the aggregated ACP (stage C_{IV}) after 2 h maturation, the inset SAED pattern in (d) shows the presence of Ca-P single crystals. (e–k) Amel-mediated formation of HAP nanorods by a characteristic multistep co-assembly process. (e) Prenucleation Ca-P clusters approximately 1.0 nm in diameter in stage A_I are detected and highlighted by arrows, and (f) 2.0–10.0 nm Ca-P clusters in stage A_{II} are observed. (g) Nanocrystalline lattices are present in these larger Ca-P clusters following continuous TEM irradiation in the high-magnification image. (h) At stage A_{III}, nanoparticles with sizes ~30–50 nm co-assemble into elongated pearl-like nanochains. All samples collected in Stages I–III were amorphous. (i) After a 2 h growth period (stage A_{IV}), bundles of ribbon-like crystals with preferentially oriented *c*-axes along the long axes of the ribbon-like microstructures are formed. The inset SAED pattern confirmed that this ribbon-like structure was HAP. (j) Extending the maturation to 24 h in stage A_{IV}, well aligned but separated nanorods underwent fusion into larger nanorods. (k) HRTEM image taken from the rectangle in (j), revealing that the measured lattice spacing ~0.346 nm corresponds to the (002) HAP lattice plane, indicating preferential alignment of the HAP crystals with their *c* axes along the long axis of the nanorods shown by the arrow in (j). This result is consistent with the inset SAED pattern in (j).

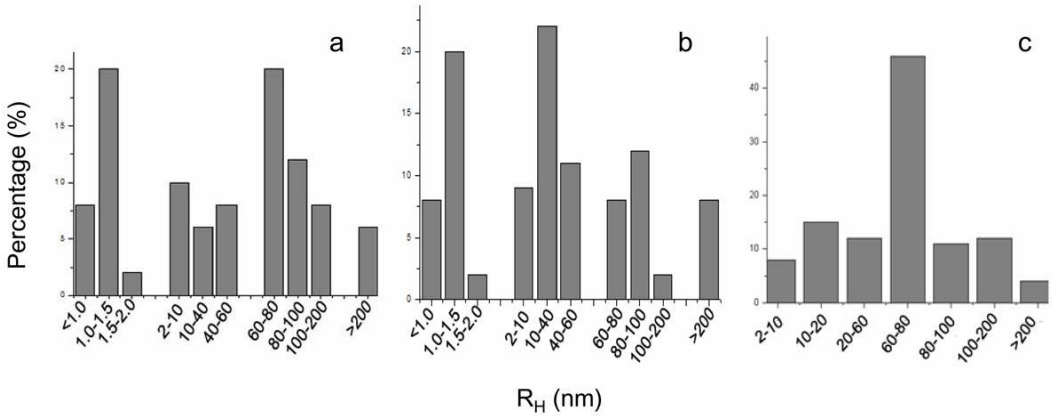

Figure 5.

Particle size distribution of Amel-Ca-P nanocluster mixtures by dynamic light scattering (DLS). (a) 25 μg mL^{-1} Amel in supersaturated Ca-P solution, Stage A_I, (b) 25 μg mL^{-1} Amel in supersaturated Ca-P solution, Stage A_{II}, and (c) 25 μg mL^{-1} Amel without Ca and P in solution. DLS is not shown for the supersaturated Ca-P solution without Amel because stable nanoclusters were not present.

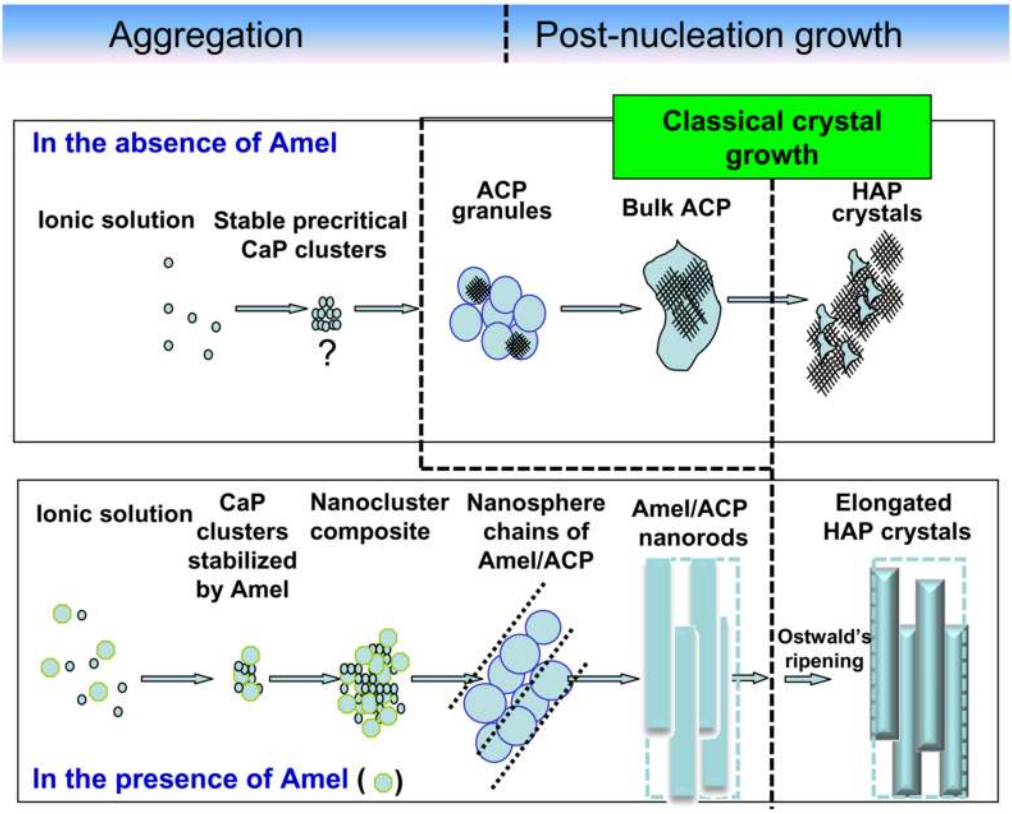

Figure 6.
Suggested mechanism for *in vitro* hierarchically organized, elongated HAP microstructures formed by co-assembly of Amel-Ca-P nanoclusters.